AIAA SciTech Forum
January 3-7, 2022, San Diego, CA & Virtual
AIAA SCITECH 2022 Forum

10.2514/6.2022-1948

Check for updates

Flow Control with Traveling-Wave Surface Morphing at Post-Stall Angles of Attack

U. E. Ogunka*,A. M. Akbarzadeh †, I. Borazjani.‡
J. Mike Walker '66 Department of Mechanical engineering, Texas A& M University, College Station, TX, 77840

Large-eddy simulations (LES) over a NACA0018 airfoil at a low Reynolds number (Re = $50,000$**) fluid flow are performed to investigate the effect of active flow control at different angles of attack (AOA =** $10°$ **to** $20°$**) using low amplitude surface morphing backward (opposite to the airfoil's forward motion) traveling wave actuation on the suction (upper) side of the airfoil. The curvilinear immersed boundary (CURVIB) method is used to handle the moving surface of the airfoil. While our previous simulations indicated the effectiveness of traveling waves at near stall angle of attack (AOA =** $15°$**), the effectiveness of these waves at post-stall AOA such as AOA =** $20°$ **is not understood. The actuation amplitude of the surface morphing traveling waves is** $a^* = 0.001$ **(**$a^* = a/L$**,** a**: amplitude,** L**: chord length of the airfoil) and the range of the reduced frequency (**$f^* = fL/U$**,** f **: frequency,** U**: free stream velocity) is from** $f^* = 4$ **to** 16**. The results of the simulations at the post-stall angle of attack (AOA =** $20°$**) show that the lift coefficient,** C_L**, increases by about** 23% **and the drag coefficient,** C_D**, decreases by about** 54% **within the frequency range from** $f^* = 8$ **to** $f^* = 10$**.**

Nomenclature

a = maximum amplitude of oscillation

a^* = nondimensional amplitude of oscillation, a/L

C = wave speed, λf

C^* = nondimensional wave speed, C/U

$\overline{C_D}$ = mean drag coefficient, $\overline{F}_D/0.5\rho U^2 L$

$\overline{C_f}$ = mean skin friction coefficient

*PhD student, J. Mike Walker '66 Department of Mechanical engineering, Texas A& M University, College Station, TX
†PhD candidate, J. Mike Walker '66 Department of Mechanical engineering, Texas A& M University, College Station, TX
‡Associate Professor, J. Mike Walker '66 Department of Mechanical engineering, Texas A& M University, College Station, TX

Copyright © 2022 by the American Institute of Aeronautics and Astronautics, Inc. All rights reserved.

Downloaded by TEXAS A & M UNIVERSITY on September 12, 2022 | http://arc.aiaa.org | DOI: 10.2514/6.2022-1948

$\overline{C_L}$ = mean lift coefficient, $\overline{F}_L/0.5\rho U^2 L$

$\overline{C_p}$ = mean pressure coefficient

δt = time step

f = frequency

f^* = reduced frequency, fL/U

$\overline{F}_D$ = mean lift force per airfoil unit span acting along the X direction

$\overline{F}_L$ = mean lift force per airfoil unit span acting along the Y direction

L = chord length of the airfoil

P = fluid pressure

Re = Reynolds number, UL/ν

s = airfoil span length, $0.1L$

U = free stream velocity

λ = wavelength

λ^* = nondimensional wavelength, λ/L

ρ = fluid density

ν = kinematic viscosity

Downloaded by TEXAS A & M UNIVERSITY on September 12, 2022 | http://arc.aiaa.org | DOI: 10.2514/6.2022-1948

I. Introduction

The study of flow separation control is of extreme importance to the aircraft industry. At low Reynolds number ($Re < 500,000$), a laminar boundary layer forms on the upper (suction) surface of the airfoil which is prone to separate from the upper (suction) surface of the airfoil either with or without turbulent reattachment depending on the angle of attack [1–3]. When the angle of attack increases towards the stall angle of the airfoil, the adverse pressure gradient on the suction side of the airfoil increases [4]. The flow separation point moves upstream as it is displaced towards the leading edge [1, 4]. The adverse pressure gradient continues to increase to a certain point, at which the flow boundary layer will separate near the leading edge on the suction side [4]. As the angle of attack increases near the stall angle, the lift coefficient increases until it reaches the maximum lift coefficient [1, 5–8]. After which, there is a significant drop in the lift of the airfoil [5, 9], where the stall occurs.

Downloaded by TEXAS A & M UNIVERSITY on September 12, 2022 | http://arc.aiaa.org | DOI: 10.2514/6.2022-1948

Distinct active flow control techniques such as steady blowing [10, 11], periodic suction and blowing [12–17], synthetic jets (zero net mass flux) [18, 19], and surface morphing [20–22] have been applied to improve the aerodynamic performance of airfoils at different AOA, including stall and post-stall AOA. The surface morphing technique is described as an energy efficient technique using light piezoelectric actuators [23], fixed along the upper surface of the airfoil. These actuations can be in the form of standing wave [20, 22, 24] or traveling wave vibrations[25–31]. Munday et al., [22] experimentally investigated the effect of a simple vibration morphing actuated on the suction side of a NACA4415 airfoil at low Re of $25,000$ and $50,000$, and angle of attack range of $0^\circ - 9^\circ$. They observed that the surface morphing simple vibration with an amplitude ($a = 0.002L; L$ = chord length of the airfoil) on the suction side of the airfoil reduced the size of the flow separation by $30 - 60\%$. Jawahar et al. [32] experimentally studied the effect of morphing trailing edge flaps for a NACA0012 at Re= $350,000$ for AOA, -5^o <AOA< 20^o. They observed trailing edge morphing flaps could improve the lift by at most 13% near the stall angle. However, this came at the expense of the drag which underwent a 14% increase at the stall angle of attack. Jones et al., [3] experimentally investigated the flow control around a NACA4415 airfoil using standing waves morphing at Re = $50,000$ and angle of attack range of $0^\circ - 16^\circ$. They observed that applying a high frequency standing wave actuation resulted in the significant reduction of the flow separation, decrease in the drag and increase in the lift compared to the non-actuated case. The studies above dealt with active flow control surface morphing in the form of standing waves, simple vibration, and flaps. However, there is little known about active flow control via traveling waves. Traveling waves have been created recently using piezoelectric actuators on structures [33]. The idea of using traveling waves for the exact purpose of flow control originates from the observation of aquatic swimmers in nature [31, 34–36]. Aquatic swimmers increase the flow momentum near their body by deforming their bodies in the form of a traveling wave [34, 35]. The flow separation of a turbulent boundary layer can be reduced via traveling waves in a channel [37, 38].

In recent work on flow control with traveling waves, the role of reduced frequency has been probed in the numerical simulations of a NACA0018 airfoil near the stall angle of incidence [26, 27, 29]. Akbarzadeh and Borazjani [26] showed that traveling waves are more effective than standing waves in terms of drag reduction and decreasing of flow separation at near stall condition (AOA = 15°) owing to the fact that traveling waves can enhance the fluid momentum directly. Ogunka et al., [29] expanded on the work of Akbarzadeh and Borazjani [26] by numerically investigating the range of amplitude $4 \times 10^{-3} > a^* > 6 \times 10^{-5}$ at high reduced frequency range $20.0 > f^* > 4.0$ for the exact purpose

of optimal flow control of a NACA0018 airfoil at near stall condition (AOA = 15°). They observed that the stall was suppressed and flow reattachment occurred at the amplitude range of $0.001 \leq a^* \leq 0.004$ at constant reduced frequency $f^* = 8$. Flow reattachment was also observed for the reduced frequency range of $8 \leq f^* \leq 12$ at constant amplitude $a^* = 0.001$. They observed that decreasing the amplitude below $a^* = 0.001$ or decreasing the reduced frequency below $f^* = 8$ led to flow separation. This might be because of the reduction of the streamwise fluid momentum due to the decrease in the amplitude (a^*) and reduced frequency (f^*)[39]. The fluid momentum scales with $(a^* f^*)^2(1 - 1/C^{*^2})$ [40]. Decreasing the reduced frequency (f^*) would reduce the wave speed ($C = \lambda f$), thereby increasing the flow separation [39, 40]. This is because the nondimensional wave speed ($C^* = \lambda^* f^*$) depends on the reduced frequency (f^*) and nondimensional wavelength (λ^*) [40]. In addition to direct increase of momentum, traveling waves can trigger instabilities (Kelvin-Helmholtz instabilities) that tend to reattach the flow. It was found that frequencies outside the range of shedding frequencies at the leading edge did not reattach the flow [29].

The above findings suggest that traveling waves can improve the aerodynamic performance and reduce the flow separation at near stall angles of attack. Nonetheless, there remains ambiguity in the understanding of the aerodynamic performance of traveling waves at post-stall angles of attack (AOA $\geq$ 18°) because of the unsteady flow characteristics that occur at post-stall angles of attack [4]. Therefore, this paper is focused on investigating the flow characteristics and aerodynamic performance (lift and drag) of the NACA0018 airfoil at post-stall angle of attack (AOA = 20°).

This paper is organized as follows: the governing equations, computational mesh, and numerical methods are described in Section II. The aerodynamic performance of the NACA0018 airfoil is quantified by measuring the mean lift and drag coefficients of the NACA0018 airfoil. The results of the lift and drag coefficient of the NACA0018 airfoil for different frequencies are compared against an baseline NACA0018 airfoil at AOA = 10°, 15° and 20° (Section III). The flow characteristics of the NACA0018 airfoil is analysed by visualizing the spanwise vorticity flow field on the suction side of the airfoil (Section III). Finally, the results are discussed, and the conclusions are reported in Section IV.

II. Method

The numerical simulations for a NACA0018 airfoil at different angles of attack (AOA = 10° − 20°) are compared. The structure of the simulation and the numerical method employed for solving the problem are similar to our previous publications [26, 27, 29]. The free stream velocity (U) and the airfoil chord length (L) are, respectively, the characteristic velocity and length, and $Re = UL/\nu = 50,000$, where ν is the kinematic viscosity. The upper (suction) surface of the

Downloaded by TEXAS A & M UNIVERSITY on September 12, 2022 | http://arc.aiaa.org | DOI: 10.2514/6.2022-1948

airfoil is prescribed with a backward (opposite to the airfoil's forward motion) traveling wave oscillation as shown in Fig. 1a. The location of the upper side of the airfoil is defined in a local frame (X, Y, Z) with its origin at the leading edge. The backward traveling wave oscillation ($h(X,t)$) prescribed along the Y direction, is:

$$h^*(X,t) = a^*(X)\sin(2\pi(f^*t^* - X^*/\lambda^*)), \tag{1}$$

where $h^* = h/L$ is the nondimensional displacement of the suction-side, $f^* = fL/U$ is the reduced frequency, $\lambda^* = \lambda/L$ is the nondimensional wavelength, $t^* = tU/L$ is the nondimensional time, $X^* = X/L$ is the nondimensional streamwise length that starts from the leading edge, and $a^*(X) = a(X)/L$ is the amplitude of the wave which starts from $X = 0.1L$ from the leading edge, to $X = 0.85L$ towards the trailing edge. The amplitude is constant and equal to its maximum value a^*_{max} from $X = 0.0L$ to $X = 0.8L$ and decreases linearly toward the trailing edge. The backward traveling wave propagates with a nondimensional wave speed, $C^* = f^*\lambda^*$, from the leading edge toward the trailing edge, and is presented in Fig. 1a. Here, the parameters with (*) symbol are nondimensional.

The flow governing equations are the three-dimensional (3D), incompressible, unsteady, filtered Navier-Stokes and continuity equations. The governing equations are discretized via a second order central scheme and integrated in time using a second-order fractional-step methodology. The momentum equations are solved with a Newton-Krylov method with an approximate analytical Jacobian solver [41], and the pressure Poisson equation is solved using GMRES solver with a multigrid preconditioner [42].

The turbulent flow is modeled using the large eddy simulation (LES) technique. A dynamic subgrid-scale model [43] is used to compute the subgrid stress tensor as previous studies [44, 45] have shown that subgrid-scale models are suitable for modeling transitional turbulent flows. The LES method is validated for modeling transitional and turbulent flows, e.g., inclined plates [40] and circular cylinders [46], and has been used in different applications such as aquatic swimming [46] and vortex flow [47]. The detail of our LES modeling can be found in previous studies [39, 48].

The computational mesh is same as previous study [26, 27], as presented in Fig.1b. The fluid domain grid is an O-grid mesh generated in curvilinear coordinates (ξ, η, ζ) where ξ is parallel to the airfoil surface and η is normal to the airfoil surface. The grid size is $421 \times 281 \times 21$ in the (ξ, η, ζ) direction. The grid is extruded in the ζ direction for $0.1L$ to generate a 3D grid domain. The radius of the O-grid shown in Fig. 1b is $15L$. Periodic boundary conditions are prescribed along the ξ and ζ directions. On the outer boundary η, the upstream is characterized by an inlet velocity

Downloaded by TEXAS A & M UNIVERSITY on September 12, 2022 | http://arc.aiaa.org | DOI: 10.2514/6.2022-1948

Downloaded by TEXAS A & M UNIVERSITY on September 12, 2022 | http://arc.aiaa.org | DOI: 10.2514/6.2022-1948

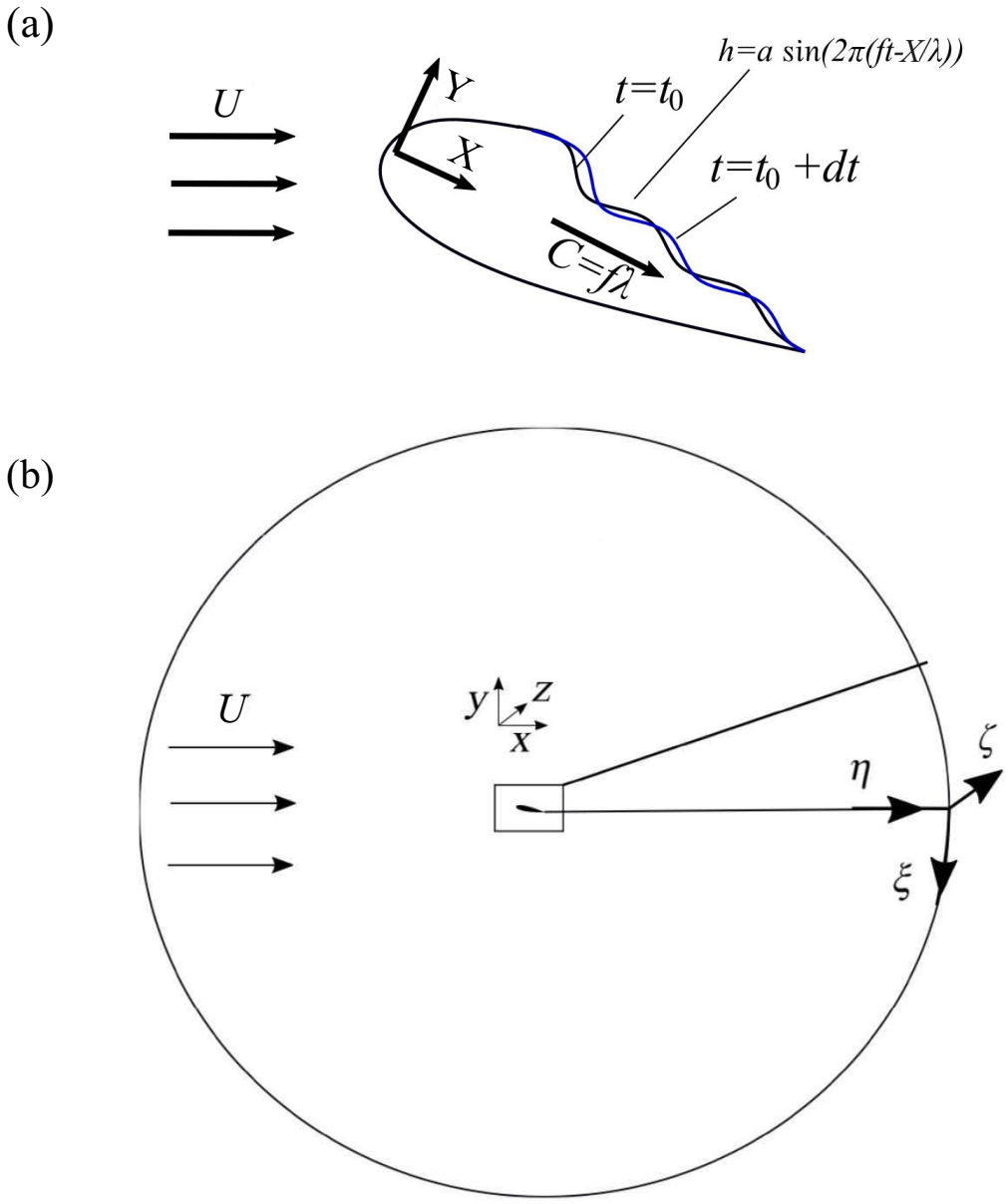

Fig. 1 (a) The schematic of backward traveling wave and (b) the simulation setup [26]

($u_X = U$) at $X < 0$, while the downstream is characterized with a Neumann boundary condition with a mass flux correction at $X > 0$. The grid resolution is maintained at $0.0003L$ along η direction near the airfoil surface that corresponds to a wall unit spacing of $\eta^+ = 0.9$ ($\eta^+ = \delta_\eta u_\tau/\nu$; δ_η is the normal distance between the first fluid node and wall surface, and u_τ is the friction velocity) for AOA = 10° - 15°. For AOA = 20°, the grid resolution is kept at $0.00019L$ along η direction with a wall unit spacing of $\eta^+ = 0.5$. The minimum grid spacing along the airfoil circumference and span are $\xi^+_{min} = 1.3$ and $\zeta^+_{min} = 13$, respectively, similar to our previous study [26]. The grid spacing is constant until

$\eta = 0.022$, then it increases with a hyperbolic function towards the boundaries. The time step is $0.0005L/U$ for all the simulations at 10°, $0.001L/U$ for the simulations at 15°, and $0.0003L/U$ for the simulations at 20°. The time step values correspond to the Courant–Friedrichs–Lewy (CFL) number, $CFL = U\delta t/\Delta x \leq 0.5$. More information on the simulation, grid sensitivity study, and validation can be found in our previous studies [26, 27, 29].

The moving boundaries are treated via the sharp curvilinear immersed boundary method (CURVIB), which is explained in the previous publications [48, 49]. The background mesh is fixed and the immersed nodes are reconstructed via an interpolation along the surface normal. A no-slip boundary condition is prescribed at the moving boundaries. The classification of the grid domain into solid, immersed, and fluid nodes is performed using the ray tracing algorithm [50]. The CURVIB method is validated for flows with moving boundaries [50] and has been applied in simulations involving turbulent flow [47], and biological flows such as aquatic locomotion [31, 46, 51, 52] and cardiovascular flows [49, 53, 54].

To quantify the aerodynamic performance of the NACA0018 airfoil, the mean lift coefficient $\overline{C}_L = \overline{F}_L/0.5\rho U^2 L$ and mean drag coefficient $\overline{C}_D = \overline{F}_D/0.5\rho U^2 L$ are computed by averaging the final 40,000 number of iterations which corresponds to about 40 time units (t^*) reported in table 1. $\overline{F}_L$ is the mean force per unit airfoil span acting along the y direction, $\overline{F}_D$ is the mean force per unit airfoil span acting along the x direction, and ρ is the fluid density.

III. Results

In this section, the aerodynamic performance (lift and drag) of the baseline and actuated NACA0018 airfoil cases are investigated and discussed in Subsection III.A at the angle of attack (AOA = 10°, 15°, and 20°). The case studies are presented in Table 1. The wavelength is kept constant at $\lambda^* = 0.44$, the same as the experimental study of Olivett et al. [25, 30]. The first and third cases are the baseline (unactuated) airfoil at AOA = 10° and 15°, respectively. Case 2^* and cases $4^{**} - 5^{**}$ are the actuated airfoils with backward surface morphing traveling waves with amplitude of $a^* = 0.001$ and frequency range of $f^* = 4 - 8$ for AOA = 10° and 15°, respectively. Case 6 is an baseline airfoil at AOA = 20°, and cases $7 - 9$ are actuated airfoils with backward traveling waves with an amplitude of $a^* = 0.001$ and frequency range of $f^* = 4 - 16$.

Downloaded by TEXAS A & M UNIVERSITY on September 12, 2022 | http://arc.aiaa.org | DOI: 10.2514/6.2022-1948

Table 1 The case studies, including baseline airfoil, backward traveling actuations with different frequencies (f^*), and angle of attacks (AOA). The amplitude (a^*) is kept constant at $a^* = 0.001$. $\overline{C_L}$ and $\overline{C_D}$ are the mean lift and drag coefficients, respectively. Here, cases with ($*$) are from the previous work of Akbarzadeh et al., [27] and cases with ($**$) are from the previous work of Ogunka et al., [29].

Case	Wave Type	f^*	a^*	$\overline{C_L}$	$\overline{C_D}$	AOA
1^*	Baseline	0	0	0.96	0.064	10°
2^*	Backward traveling wave	4.0	0.001	0.998	0.059	10°
3^{**}	Baseline	0	0	0.676	0.279	15°
4^{**}	Backward traveling wave	4.0	0.001	0.69	0.262	15°
5^{**}	Backward traveling wave	8.0	0.001	0.89	0.090	15°
6	Baseline	0	0	0.70	0.308	20°
7	Backward traveling wave	4.0	0.001	0.69	0.26	20°
8	Backward traveling wave	8.0	0.001	0.87	0.17	20°
9	Backward traveling wave	10.0	0.001	0.86	0.17	20°
10	Backward traveling wave	16.0	0.001	0.69	0.28	20°

Downloaded by TEXAS A & M UNIVERSITY on September 12, 2022 | http://arc.aiaa.org | DOI: 10.2514/6.2022-1948

A. Effect of Angle of Attack

From Table 1, the results show that an increase in the angle of attack of the baseline case from 10° pre-stall (case 1^*) to 15° stall (case 3^{**}) leads to a 30% significant reduction in C_L and a 336% significant increase in C_D. This change in the lift and drag coefficients implies that the airfoil has stalled near the 15° angle of attack, i.e., 15° is near the stall angle of the airfoil. Increasing the angle of attack to AOA = 20° post-stall for the baseline case (case 6), the lift decreases by 27% and the drag increases by 381% compared to the baseline case 1^* at 10° pre-stall. A low amplitude ($a^* = 0.001$) traveling wave oscillation, with frequency $f^* = 4$, applied at AOA=10° increases C_L by about 4% and decreases the C_D by about 8% compared to the baseline case 1^*. The result of this actuation is very similar to the baseline case at AOA = 10°, which indicates that the actuation is seemingly ineffective in making significant changes to the flow characteristics at AOA = 10°, a point further shown in Fig. 4a and Fig. 4b. However, this is not the case for AOA = 15° − 20°. At $f^* = 4$ and $a^* = 0.001$, the C_L increases by about 1.6% and decreases the C_D by about 1.4% compared to the baseline case 3^{**}. Increasing the frequency to $f^* = 8$ and keeping the amplitude constant, C_L increases by about 32% and C_D decreases by about 68% compared to the baseline case 3^{**}. At AOA = 15°, the frequency increase from $f^* = 4$ to $f^* = 8$ caused a significant increase in the lift and significant reduction of the drag of the airfoil. This suggests that a backward traveling wave surface morphing actuation of $a^* = 0.001$ and $f^* = 8$ will enhance the aerodynamic performance of the airfoil at the near stall angle of attack. From Table 1, the maximum lift coefficient and minimum drag coefficient occur at AOA = 10°. However, the highest percentage change between the baseline and actuated airfoil occurred at AOA =

15°. From our previous works, the optimal range of the surface morphing wave parameters (frequency and amplitude) on the aerodynamic performance (lift and drag) of the airfoil are $f^* = 2 - 8$ and $a^* = 0.001 - 0.002$ at AOA = 10° and $f^* = 8 - 12$ and $a^* = 0.001 - 0.004$ at AOA = 15°. Increasing the angle of attack to post-stall (AOA = 20°) and applying the traveling wave actuation at $f^* = 4$ or $f^* = 16$ and $a^* = 0.001$, the C_L decreases by about 2% and decreases the C_D by about 28% compared to the baseline case 6. Increasing the frequency to $f^* = 8 - 10$ and keeping the amplitude constant, C_L significantly increases by about 23% and the C_D significantly decreases by about 54% compared to the baseline case 6.

Downloaded by TEXAS A & M UNIVERSITY on September 12, 2022 | http://arc.aiaa.org | DOI: 10.2514/6.2022-1948

1. Aerodynamic Performance of the Baseline and Actuated Airfoils

Figures 2a and 2b present the lift and drag curves of the baseline and actuated ($f^* = 8.0, a^* = 0.001$) airfoils. The lift coefficient, C_L, of the baseline airfoil linearly increases with increasing low angles of attack, AOA = $0^0 - 10^0$. The maximum value of the lift coefficient of the baseline airfoil is reached at AOA = 10^0, after which stall occurs at AOA = 15^0. C_L significantly reduces at AOA = 15^0, but slightly increases as the angle of attack increases to AOA = 20^0 post-stall. The drag curve of the baseline airfoil show that C_D slightly increases as the angle of attack increases for low angles of attack (AOA = $0^0 - 10^0$) but significantly increases as the angle of attack approaches AOA = 15^0 (stall angle) and continues to increase post-stall (AOA = 20^0). The actuated airfoil at AOA = 10^0 angle of attack observed an increase in C_L of 4% and a C_D reduction of 9% compared to the baseline airfoil as shown in Figs. 2a and 2b. This suggests that no significant changes in the aerodynamic performance of the airfoil occurred at AOA = 10° compared to the baseline airfoil. Nevertheless, at the stall (AOA = 15^0) and post-stall (AOA= 20^0) angles of attack for the actuated airfoil, the lift coefficient (C_L) significantly increases by at least 23%, and the drag coefficient (C_D) significantly reduces by at least 54% compared to the baseline airfoil.

2. Effect of Frequency at Post-Stall

Here, the effect of frequency at post-stall (AOA = 20^0) is investigated. Figures 3a and 3b show the effect of frequency of the traveling wave actuation on the aerodynamic performance (lift and drag) of the NACA0018 airfoil with the actuation amplitude set to $a^* = 0.001$. The lift coefficient, C_L, reduces by 2% at $f^* = 4$ and $f^* = 16$, but significantly increases to 23% at $f^* = 8 - 10$ compared to the baseline airfoil. The drag coefficient, C_D, reduces by at most 28% at $f^* = 4$ and $f^* = 16$ compared to the baseline airfoil. However, we observe a significant decrease of 54% in the drag

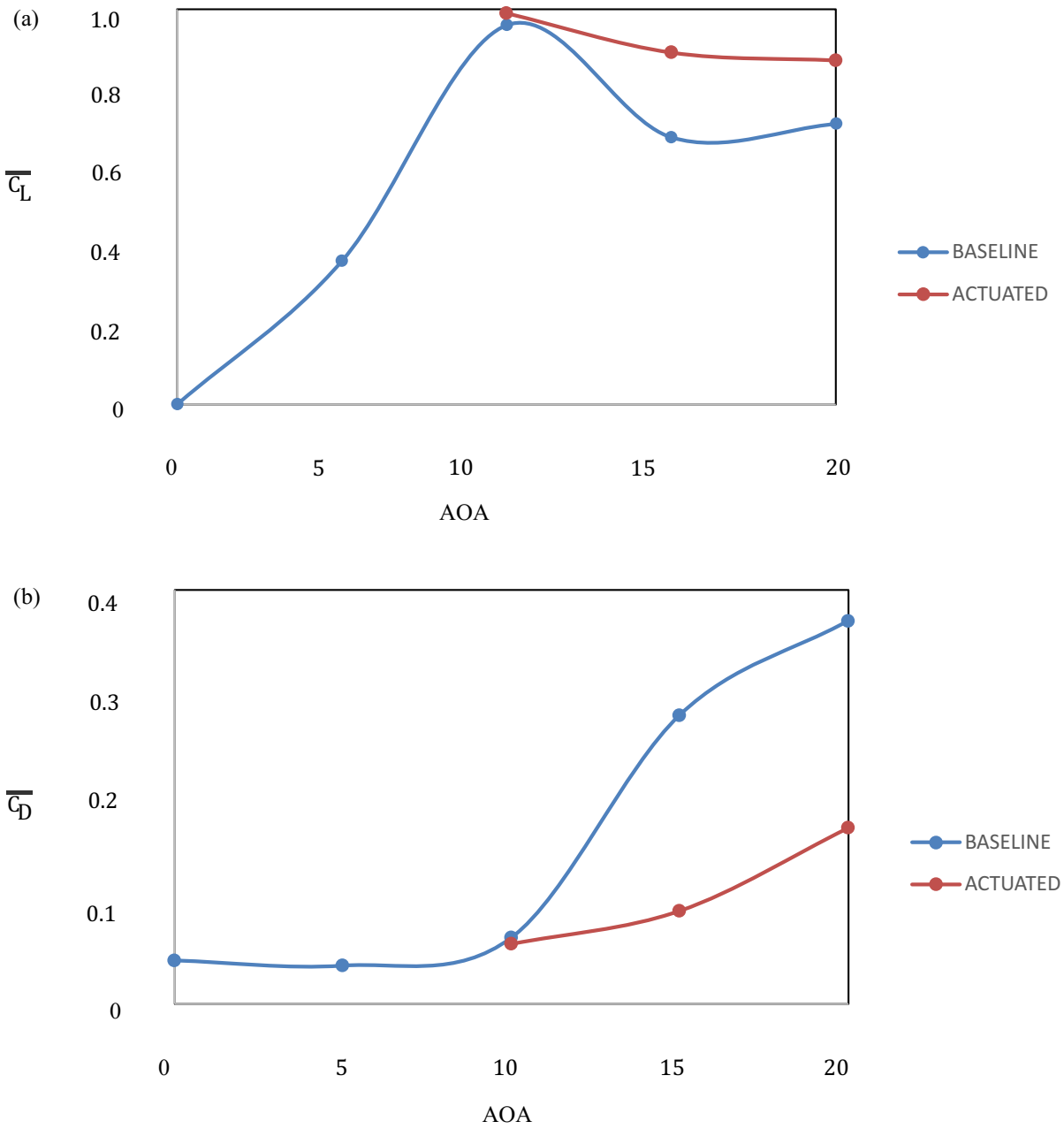

Fig. 2 Evolution of the (a) lift (C_L) and (b) drag (C_D) curves of the baseline and actuated $(f^* = 8.0, a^* = 0.001)$ airfoil for AOA = $0^0 - 20^0$.

coefficient at $f^* = 8 - 10$ compared to the baseline airfoil. Therefore, the The max lift and min drag coefficients were observed at the range of the reduced frequency, $f^* = 8 - 10$.

3. Flow Visualization

The effects of the actuation deformation on the flow development around the airfoil for all the cases listed in table 1 above can be observed by the distribution of the contours of the instantaneous spanwise vorticity profile around the

Downloaded by TEXAS A & M UNIVERSITY on September 12, 2022 | http://arc.aiaa.org | DOI: 10.2514/6.2022-1948

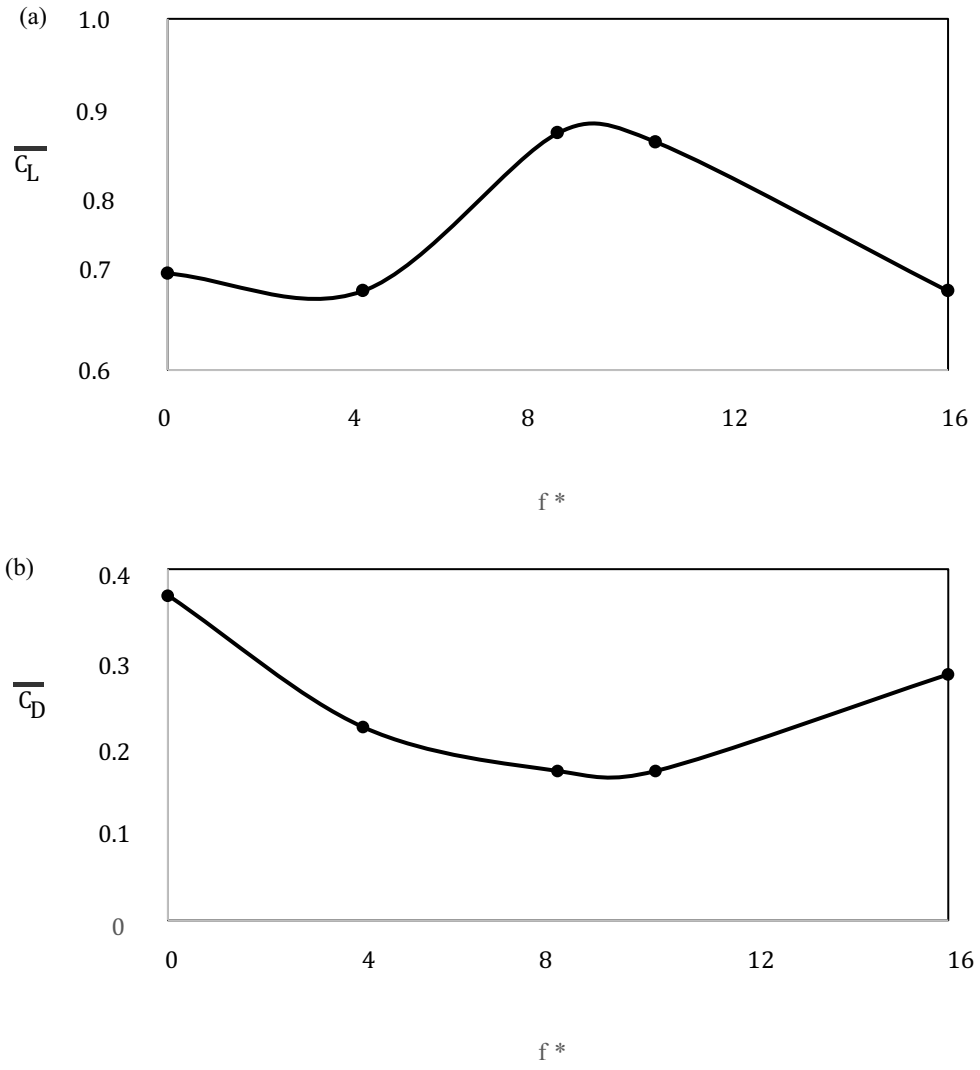

Fig. 3 Effect of frequency of the traveling wave on the (a) lift coefficient (C_L) and (b) drag coefficient (C_D) of an airfoil for AOA = 20^0 with amplitude $a^* = 0.001$.

airfoil NACA0018 at three different angles of attack (AOA = 10°, 15° and 20°) in Fig. 4. Each case is visualized at four different phases of the trailing edge vortex shedding cycle. For case 1^* at AOA = 10°, the flow boundary layer remains attached from the leading edge of the airfoil. There is a periodic formation of small vortices near the trailing edge [55]. Applying a backward traveling wave actuation with $f^* = 4$ and $a^* = 0.001$ in case 2^* does not seem to have any significant effect on the flow structure as the flow field is similar to that of case 1^*. There is no significant change in the size or location of the boundary layer region or trailing edge vortex compared to the baseline case 1^*. On the other hand, increasing the angle of attack to 15° with no actuation in case 3^{**}, the flow boundary layer separates from the leading edge and a large recirculatory zone is formed near the trailing edge. A large vortex is also shed continuously

Downloaded by TEXAS A & M UNIVERSITY on September 12, 2022 | http://arc.aiaa.org | DOI: 10.2514/6.2022-1948

Downloaded by TEXAS A & M UNIVERSITY on September 12, 2022 | http://arc.aiaa.org | DOI: 10.2514/6.2022-1948

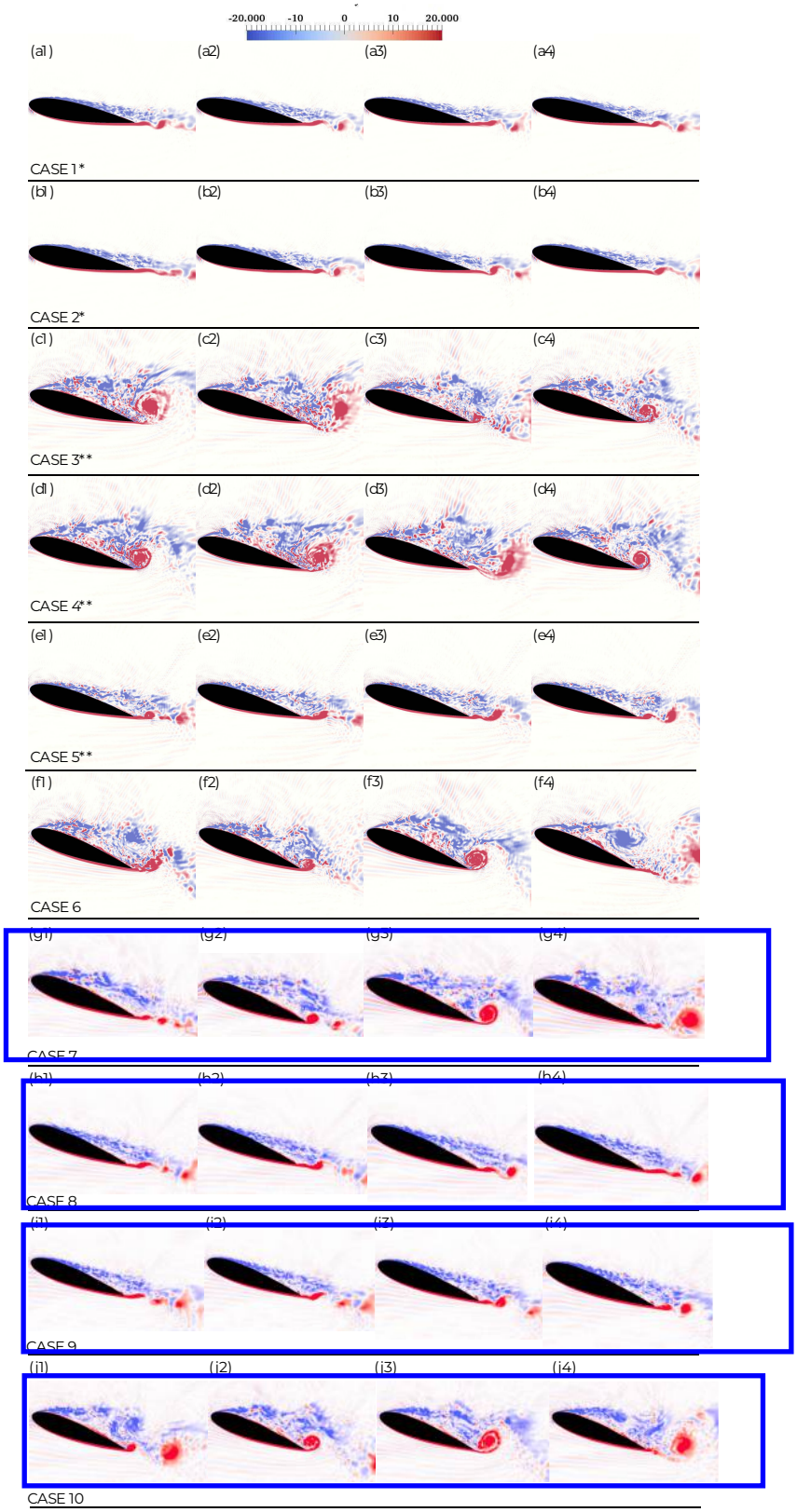

Fig. 4 The contours of the instantaneous spanwise vorticity.

Downloaded by TEXAS A & M UNIVERSITY on September 12, 2022 | http://arc.aiaa.org | DOI: 10.2514/6.2022-1948

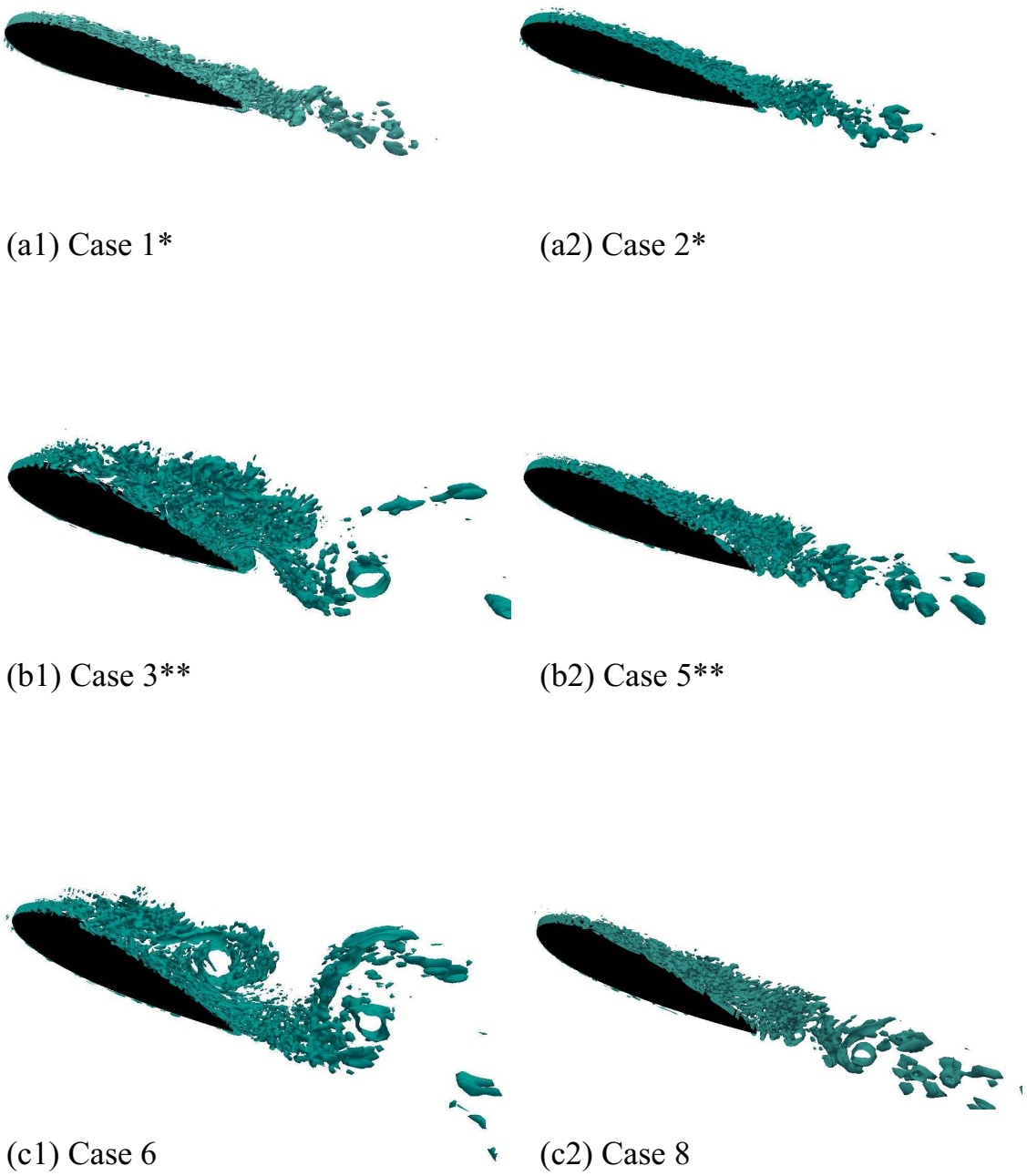

Fig. 5 Three dimensional (3D) vortical structures visualized by the isosurface of Q-criterion (Q=20) of the NACA0018 airfoil (a1) baseline case and (a2) actuated case ($f^* = 4$ and $a^* = 0.001$) at AOA = 10°, b1) baseline case and (b2) actuated case ($f^* = 8$ and $a^* = 0.001$) at AOA = 15°, c1) baseline case and (c2) actuated case ($f^* = 8$ and $a^* = 0.001$) at AOA = 20°.

near the trailing edge. Despite applying a backward traveling wave actuation with $f^* = 4$ and $a^* = 0.001$ in case 4^{**} at this angle of attack, AOA = 15°, the flow field remains relatively similar to that of case 3^{**} as can be observed in Fig.4. However, by increasing the frequency of the oscillation to $f^* = 8$ and keeping the amplitude at $a^* = 0.001$ in case 5^{**} (Fig.4), the flow boundary layer is reattached on the leading edge of the airfoil and the large recirculatory zone is eliminated. The separated flow has been suppressed, the stall has been delayed, and the highest lift enhancement and drag reduction are observed. This suggests that a backward traveling wave surface morphing actuation of $a^* = 0.001$ and $f^* = 8$ will enhance the aerodynamic performance of the airfoil at the near stall angle of attack. Further increasing the angle of attack to 20° with no actuation in case 6, the flow boundary layer remains separated from the leading edge, with a large vortex generated at the trailing edge as shown in Fig. 4. This formation and shedding of the vortex at the trailing edge leads to the decrease of the lift and stall of the airfoil. Similarly to the stall angle of 15°, applying a backward traveling wave actuation with $f^* = 4$ and $a^* = 0.001$ in case 7 at this angle of attack, AOA = 20°, the flow field remains relatively similar to the baseline airfoil (case 6) as can be observed in Fig.4. Nevertheless, by increasing the frequency of the oscillation to $f^* = 8 - 10$ and keeping the amplitude at $a^* = 0.001$ in cases $8 - 9$ (Fig.4), the flow boundary layer is reattached on the suction side of the airfoil, stall is suppressed, and the large vortex shedding at the trailing edge is diminished. The maximum lift enhancement and drag reduction at post-stall, AOA = 20°, are observed. This suggests that a backward traveling wave surface morphing actuation of $a^* = 0.001$ and $f^* = 8 - 10$ will enhance the aerodynamic performance of the airfoil at post-stall angle of attack. However, increasing the reduced frequency to $f^* = 16$ (case 10), the flow field is separated and a large recirculatory zone is formed at the trailing edge, similar to the baseline airfoil (case 6).

The three dimensional (3D) instantaneous vorticity contours visualized by means of the iso-surfaces of the Q-criterion [56] for the baseline case (case 1^*) and actuated case (case 2^*) at AOA = 10°, baseline case (case 3^{**}) and actuated case (case 5^{**}) at AOA = 15°, and baseline case (case 6) actuated case (case 8) at AOA = 20° are shown in Fig. 5. From Fig. 5a1, the flow remains reattached to the leading edge of the suction side of the airfoil at AOA = 10°. The actuation of $f^* = 4$ and $a^* = 0.001$ applied at AOA = 10° does not make any major change to the size and structure of the flow boundary layer as shown in Fig. 5a2. At AOA = 15°, the flow starts to separate near the leading edge of the airfoil and fails to reattach to the airfoil surface, shown in Fig. 5b1. The laminar separation bubble (LSB) bursts at the near stall angle of attack (AOA= 15°) [57]. The separation is characterized by a large recirculation zone occurring

Downloaded by TEXAS A & M UNIVERSITY on September 12, 2022 | http://arc.aiaa.org | DOI: 10.2514/6.2022-1948

on the suction side of the airfoil. Large shedding vortices are formed behind the trailing edge of the airfoil due to the interaction between the structures separated from the turbulent shear layer and the incoming flow along the pressure side of the airfoil. In Fig. 5b2, a backward traveling wave actuation of $f^* = 8$ and $a^* = 0.001$ on the suction side of the airfoil is applied and the flow separation near the leading edge of the airfoil is reduced significantly at AOA = 15°. Then, flow reattachment occurs immediately near the leading edge of the airfoil, with the fully turbulent flow moving downstream to the trailing edge. Increasing the angle of attack to AOA = 20°, the flow boundary layer on the suction side of the airfoil still separates near the leading edge, with a large trailing edge vortex and a large recirculation zone on the suction side of the airfoil as shown in Fig. 5c1. In Fig. 5c2, a backward traveling wave actuation of $f^* = 8$ and $a^* = 0.001$ on the suction side of the airfoil is applied and the flow separation near the leading edge of the airfoil is reduced significantly at AOA = 20°, similar to that shown in Fig. 5b2. Flow reattachment occurred near the leading edge of the airfoil and the large recirculatory zone at the trailing edge is eliminated. This effect is similar to those observed in the two dimensional (2D) flow of the vorticity contours presented in Fig. 4.

Downloaded by TEXAS A & M UNIVERSITY on September 12, 2022 | http://arc.aiaa.org | DOI: 10.2514/6.2022-1948

IV. Conclusion

This study provides a quantification of the aerodynamic performance of the effect of low amplitude traveling wave surface morphing with different reduced frequencies on the airfoil NACA0018 at different angles of attack (AOA = 10°, 15°, and 20°) at Re = 50, 000 using Large-eddy simulations (LES). The effect of backward traveling waves with various reduced frequencies, ranging from $f^* = 4$ to $f^* = 16$, are investigated on the flow separation and aerodynamic performance of a NACA0018 airfoil at different angles of attack (AOA = 10°, 15°, and 20°).

Flow separation occurred at the stall and post-stall angles of attack (AOA = 15° and 20°). The lift and drag coefficients, C_L and C_D increased as the angle of attack (AOA) increased. The lift coefficient, C_L, significantly decreases as the NACA0018 airfoil reached the stall angle of attack (AOA = 15°). The plots of C_L and C_D profiles, and the contours of the instantaneous spanwise vorticity profile of the flow field suggest that the actuation oscillation does not have a significant effect on the lift and drag of the airfoil at the pre-stall angle of attack, AOA = 10°. However, at the near stall AOA = 15°, the maximum lift enhancement and drag reduction is achieved when applying a backward traveling wave actuation with a reduced frequency of $f^* = 8$ and an actuation amplitude of $a^* = 0.001$. At these values, a maximum lift increase of 32% and drag decrease of 68% occurred at 15°. Similarly, the maximum lift enhancement and drag reduction were achieved with a reduced frequency range of $f^* = 8 - 10$ and an actuation amplitude of $a^* = 0.001$

at post-stall angle of attack (AOA = 20°). The lift significantly increased by 23% and the drag significantly decreased by 54%. At these values, the flow was reattached to the suction side of the airfoil at post-stall (AOA = 20°). Therefore, low amplitude ($a^* = 0.001$) backward traveling wave actuations suppressed the stall at AOA = 15° and 20°.

.

Acknowledgments

This work was partly supported by the National Science Foundation (NSF) grant CBET 1905355. The computational resources were partly provided by the High Performance Research Computing (HPRC) facilities at Texas A&M University.

Downloaded by TEXAS A & M UNIVERSITY on September 12, 2022 | http://arc.aiaa.org | DOI: 10.2514/6.2022-1948

References

[1] Gerakopulos, R., Boutilier, M., and Yarusevych, S., "Aerodynamic characterization of a NACA 0018 airfoil at low Reynolds numbers," *40th Fluid dynamics conference and Exhibit*, 2010, p. 4629.

[2] Greenblatt, D., and Wygnanski, I. J., "The control of flow separation by periodic excitation," *Progress in aerospace Sciences*, Vol. 36, No. 7, 2000, pp. 487–545.

[3] Jones, G., Santer, M., and Papadakis, G., "Control of low Reynolds number flow around an airfoil using periodic surface morphing: A numerical study," *Journal of Fluids and Structures*, Vol. 76, 2018, pp. 95–115.

[4] Timmer, W., and Bak, C., "Aerodynamic characteristics of wind turbine blade airfoils," *Advances in wind turbine blade design and materials*, Elsevier, 2013, pp. 109–149.

[5] Young, A., "Aerodynamics. By LJ CLANCY. Pitman, 1975. 610 pp.£ 10.00." *Journal of Fluid Mechanics*, Vol. 77, No. 3, 1976, pp. 623–624.

[6] Timmer, W., "Two-dimensional low-Reynolds number wind tunnel results for airfoil NACA 0018," *Wind engineering*, Vol. 32, No. 6, 2008, pp. 525–537.

[7] Kumar, V., Paraschivoiu, M., and Paraschivoiu, I., "Low Reynolds number vertical axis wind turbine for Mars," *Wind Engineering*, Vol. 34, No. 4, 2010, pp. 461–476.

[8] Raghunathan, S., and Ombaka, O., "A thick symmetrical aerofoil oscillating about zero incidence angle," *International journal of heat and fluid flow*, Vol. 7, No. 2, 1986, pp. 155–159.

[9] Crane, D., and Team, A. E., *Dictionary of Aeronautical Terms: Over 11,000 Entries*, Aviation Supplies & Academics, Incorporated, 2012.

[10] Aubrun, S., McNally, J., Alvi, F., and Kourta, A., "Separation flow control on a generic ground vehicle using steady microjet arrays," *Experiments in Fluids*, Vol. 51, No. 5, 2011, pp. 1177–1187. https://doi.org/10.1007/s00348-011-1132-0.

[11] Donovan, J., Kral, L., and Cary, A., "Active flow control applied to an airfoil," *36th AIAA Aerospace Sciences Meeting and Exhibit*, American Institute of Aeronautics and Astronautics, 1998. https://doi.org/10.2514/6.1998-210.

[12] Greenblatt, D., and Wygnanski, I. J., "The control of flow separation by periodic excitation," *Progress in aerospace Sciences*, Vol. 36, No. 7, 2000, pp. 487–545.

[13] Seifert, A., Darabi, A., and Wyganski, I., "Delay of airfoil stall by periodic excitation," *Journal of Aircraft*, Vol. 33, No. 4, 1996, pp. 691–698. https://doi.org/10.2514/3.47003.

[14] WU, J.-Z., LU, X.-Y., DENNY, A. G., FAN, M., and WU, J.-M., "Post-stall flow control on an airfoil by local unsteady forcing," *Journal of Fluid Mechanics*, Vol. 371, 1998, pp. 21–58. https://doi.org/10.1017/s0022112098002055.

[15] Glezer, A., and Amitay, M., "Synthetic jets," *Annual review of fluid mechanics*, Vol. 34, No. 1, 2002, pp. 503–529.

[16] Amitay, M., Smith, D. R., Kibens, V., Parekh, D. E., and Glezer, A., "Aerodynamic Flow Control over an Unconventional Airfoil Using Synthetic Jet Actuators," *AIAA Journal*, Vol. 39, No. 3, 2001, pp. 361–370. https://doi.org/10.2514/2.1323.

[17] Buchmann, N. A., Atkinson, C., and Soria, J., "Influence of ZNMF jet flow control on the spatio-temporal flow structure over a NACA-0015 airfoil," *Experiments in Fluids*, Vol. 54, No. 3, 2013. https://doi.org/10.1007/s00348-013-1485-7.

[18] Rodríguez Pérez, I. M., Lehmkuhl, O., and Borrell Pol, R., "Effects of the actuation on the boundary layer of an airfoil at Reynolds Number Re= 60000," *Flow turbulence and combustion*, 2020, pp. 1–20.

[19] Glezer, A., "Some aspects of aerodynamic flow control using synthetic-jet actuation," *Philosophical Transactions of the Royal Society A: Mathematical, Physical and Engineering Sciences*, Vol. 369, No. 1940, 2011, pp. 1476–1494.

[20] Jones, G., Santer, M., Debiasi, M., and Papadakis, G., "Control of flow separation around an airfoil at low Reynolds numbers using periodic surface morphing," *Journal of Fluids and Structures*, Vol. 76, 2018, pp. 536–557.

[21] Park, Y. W., Lee, S.-G., Lee, D.-H., and Hong, S., "Stall Control with Local Surface Buzzing on a NACA 0012 Airfoil," *AIAA Journal*, Vol. 39, No. 7, 2001, pp. 1400–1402. https://doi.org/10.2514/2.1460.

Downloaded by TEXAS A & M UNIVERSITY on September 12, 2022 | http://arc.aiaa.org | DOI: 10.2514/6.2022-1948

[22] Munday, D., and Jacob, J., "Active Control of Separation on a Wing with Oscillating Camber," *Journal of Aircraft*, Vol. 39, No. 1, 2002, pp. 187–189. https://doi.org/10.2514/2.2915.

[23] Seifert, A., Eliahu, S., Greenblatt, D., and Wygnanski, I., "Use of Piezoelectric Actuators for Airfoil Separation Control," *AIAA Journal*, Vol. 36, No. 8, 1998, pp. 1535–1537. https://doi.org/10.2514/2.549.

[24] Jones, G., Santer, M., and Papadakis, G., "Control of low Reynolds number flow around an airfoil using periodic surface morphing: A numerical study," *Journal of Fluids and Structures*, Vol. 76, 2018, pp. 95–115. https://doi.org/10.1016/j.jfluidstructs.2017.09.009.

[25] Olivett, A., Corrao, P., and Karami, M., "Flow Control and Separation Delay in Morphing Wing Aircraft Using Traveling Wave Actuation," *ASME 2020 Conference on Smart Materials, Adaptive Structures and Intelligent Systems*, American Society of Mechanical Engineers Digital Collection, 2020.

[26] Akbarzadeh, A., and Borazjani, I., "Controlling flow separation on a thick airfoil using backward traveling waves," *AIAA Journal*, Vol. 58, No. 9, 2020, pp. 3799–3807.

[27] Akbarzadeh, A., and Borazjani, I., "A numerical study on controlling flow separation via surface morphing in the form of backward traveling waves," *AIAA Aviation 2019 Forum*, 2019, p. 3589.

[28] Albers, M., Meysonnat, P. S., and Schröder, W., "Actively reduced airfoil drag by transversal surface waves," *Flow, Turbulence and Combustion*, Vol. 102, No. 4, 2019, pp. 865–886.

[29] Ogunka, U., Akbarzadeh, A., and Borazjani, I., "The Role of Amplitude on Controlling Flow Separation Using Traveling Wave Morphing," *AIAA Scitech 2021*, 2021.

[30] Olivett, A., Corrao, P., and Karami, M. A., "Flow control and separation delay in morphing wing aircraft using traveling wave actuation," *Smart Materials and Structures*, Vol. 30, No. 2, 2021, p. 025028.

[31] Ogunka, U. E., Daghooghi, M., Akbarzadeh, A. M., and Borazjani, I., "The Ground Effect in Anguilliform Swimming," *Biomimetics*, Vol. 5, No. 1, 2020, p. 9.

[32] Kamliya Jawahar, H., Ai, Q., and Azarpeyvand, M., "Experimental and numerical investigation of aerodynamic performance of airfoils fitted with morphing trailing-edges," *23rd AIAA/CEAS aeroacoustics conference*, 2017, p. 3371.

[33] Bani-Hani, M., and Karami, M., "Analytical structural optimization and experimental verifications for traveling wave generation in self-assembling swimming smart boxes," *Smart Materials and Structures*, Vol. 24, No. 9, 2015, p. 094005.

Downloaded by TEXAS A & M UNIVERSITY on September 12, 2022 | http://arc.aiaa.org | DOI: 10.2514/6.2022-1948

[34] Taneda, S., "Visual study of unsteady separated flows around bodies," *Progress in Aerospace Sciences*, Vol. 17, 1976, pp. 287–348.

[35] Borazjani, I., and Sotiropoulos, F., "Numerical investigation of the hydrodynamics of carangiform swimming in the transitional and inertial flow regimes," *Journal of Experimental Biology*, Vol. 211, No. 10, 2008, pp. 1541–1558.

[36] Borazjani, I., and Sotiropoulos, F., "Numerical investigation of the hydrodynamics of anguilliform swimming in the transitional and inertial flow regimes," *Journal of Experimental Biology*, Vol. 212, No. 4, 2009, pp. 576–592.

[37] Nakanishi, R., Mamori, H., and Fukagata, K., "Relaminarization of turbulent channel flow using traveling wave-like wall deformation," *International Journal of Heat and Fluid Flow*, Vol. 35, 2012, pp. 152–159. https://doi.org/10.1016/j.ijheatfluidflow.2012.01.007.

[38] Mamori, H., Iwamoto, K., and Murata, A., "Effect of the parameters of traveling waves created by blowing and suction on the relaminarization phenomena in fully developed turbulent channel flow," *Physics of Fluids*, Vol. 26, No. 1, 2014, p. 015101. https://doi.org/10.1063/1.4851256.

[39] Akbarzadeh, A. M., and Borazjani, I., "Large eddy simulations of a turbulent channel flow with a deforming wall undergoing high steepness traveling waves," *Physics of Fluids*, Vol. 31, No. 12, 2019, p. 125107. https://doi.org/10.1063/1.5131268.

[40] Akbarzadeh, A., and Borazjani, I., "Reducing flow separation of an inclined plate via travelling waves," *Journal of Fluid Mechanics*, Vol. 880, 2019, pp. 831–863.

[41] Asgharzadeh, H., and Borazjani, I., "A Newton–Krylov method with an approximate analytical Jacobian for implicit solution of Navier–Stokes equations on staggered overset-curvilinear grids with immersed boundaries," *Journal of computational physics*, Vol. 331, 2017, pp. 227–256.

[42] Ge, L., and Sotiropoulos, F., "A numerical method for solving the 3D unsteady incompressible Navier–Stokes equations in curvilinear domains with complex immersed boundaries," *Journal of computational physics*, Vol. 225, No. 2, 2007, pp. 1782–1809.

[43] Germano, M., Piomelli, U., Moin, P., and Cabot, W. H., "A dynamic subgrid-scale eddy viscosity model," *Physics of Fluids A: Fluid Dynamics*, Vol. 3, No. 7, 1991, pp. 1760–1765.

[44] Rizzetta, D. P., Visbal, M. R., and Morgan, P. E., "A high-order compact finite-difference scheme for large-eddy simulation of active flow control," *Progress in Aerospace Sciences*, Vol. 44, No. 6, 2008, pp. 397–426.

Downloaded by TEXAS A & M UNIVERSITY on September 12, 2022 | http://arc.aiaa.org | DOI: 10.2514/6.2022-1948

[45] Akhavan-Safaei, A., Seyedi, S. H., and Zayernouri, M., "Anomalous features in internal cylinder flow instabilities subject to uncertain rotational effects," *Physics of Fluids*, Vol. 32, No. 9, 2020, p. 094107.

[46] Bottom II, R., Borazjani, I., Blevins, E., and Lauder, G., "Hydrodynamics of swimming in stingrays: numerical simulations and the role of the leading-edge vortex," *Journal of Fluid Mechanics*, Vol. 788, 2016, pp. 407–443.

[47] Asadi, H., Asgharzadeh, H., and Borazjani, I., "On the scaling of propagation of periodically generated vortex rings," *Journal of Fluid Mechanics*, Vol. 853, 2018, pp. 150–170. https://doi.org/10.1017/jfm.2018.529.

[48] Borazjani, I., and Akbarzadeh, A., "Large Eddy Simulations of Flows with Moving Boundaries," *Modeling and Simulation of Turbulent Mixing and Reaction*, Springer, 2020, pp. 201–225.

[49] Borazjani, I., Ge, L., and Sotiropoulos, F., "Curvilinear immersed boundary method for simulating fluid structure interaction with complex 3D rigid bodies," *Journal of Computational physics*, Vol. 227, No. 16, 2008, pp. 7587–7620.

[50] Borazjani, I., Ge, L., and Sotiropoulos, F., "Curvilinear immersed boundary method for simulating fluid structure interaction with complex 3D rigid bodies," *Journal of Computational physics*, Vol. 227, No. 16, 2008, pp. 7587–7620.

[51] Daghooghi, M., and Borazjani, I., "Self-propelled swimming simulations of bio-inspired smart structures," *Bioinspiration & biomimetics*, Vol. 11, No. 5, 2016, p. 056001.

[52] Daghooghi, M., Ogunka, U., and Borazjani, I., "The ground effect on anguiliform swimming performance," *APS*, 2019, pp. G03–005.

[53] Borazjani, I., "Fluid–structure interaction, immersed boundary-finite element method simulations of bio-prosthetic heart valves," *Computer Methods in Applied Mechanics and Engineering*, Vol. 257, 2013, pp. 103–116.

[54] Hedayat, M., and Borazjani, I., "Comparison of platelet activation through hinge vs bulk flow in bileaflet mechanical heart valves," *Journal of biomechanics*, Vol. 83, 2019, pp. 280–290.

[55] Nakano, T., Fujisawa, N., Oguma, Y., Takagi, Y., and Lee, S., "Experimental study on flow and noise characteristics of NACA0018 airfoil," *Journal of Wind Engineering and Industrial Aerodynamics*, Vol. 95, No. 7, 2007, pp. 511–531.

[56] Hunt, J. C., Wray, A. A., and Moin, P., "Eddies, streams, and convergence zones in turbulent flows," 1988.

[57] Alam, M., and Sandham, N. D., "Direct numerical simulation of'short'laminar separation bubbles with turbulent reattachment," *Journal of Fluid Mechanics*, Vol. 410, 2000, pp. 1–28.

Downloaded by TEXAS A & M UNIVERSITY on September 12, 2022 | http://arc.aiaa.org | DOI: 10.2514/6.2022-1948